Inertial migration of a non-neutrally buoyant particle in a linear shear flow with thermal convection

Wenwei Liu [1,2,*] and Chuan-Yu Wu [2,*]

[1]*State Key Laboratory of Multi-Phase Complex Systems, Institute of Process Engineering, Chinese Academy of Sciences, Beijing 100190, China and Nanjing IPE Institute of Green Manufacturing Industry, Nanjing 211135, China*
[2]*Department of Chemical and Process Engineering, University of Surrey, Guildford GU2 7XH, United Kingdom*

We perform numerical simulations on inertial migration of a non-neutrally buoyant particle with a density ratio of 0.98–1.02 in a linear shear flow dominated channel with a Reynolds number up to 500 in the presence of thermal convection using a double-population lattice Boltzmann method. It is found that under the isothermal condition, the particle with a larger density difference from the fluid will either settle to the bottom of the channel or float to the top of the channel, while the particle with a smaller particle-fluid density difference remains suspended in the channel due to the inertial lift force. The presence of thermal convection (characterized by the Grashof number Gr) induces an additional downward lift force, which results in distinctive migration behaviors that depend on whether the particle density is larger or smaller than that of the fluid. For a particle heavier than the fluid, the settling is enhanced by thermal convection due to the synergistic effect of the thermal lift force and the gravitational force. The critical Reynolds number for lifting the particle increases compared with the isothermal case and is linearly correlated with the dimensionless density ratio (σ). On the other hand, for a particle lighter than the fluid, an empirical dimensionless number Gr*, defined as Gr/[σ (1.59Re + 9.31)], is introduced to characterize the particle migration. It is discovered that the particle's equilibrium position depends on whether it migrates to the top wall or remains suspended in the shear flow under the isothermal condition. For the former case, when thermal convection is introduced, the particle stays at the top wall when Gr* < 1, and becomes suspended in the channel when Gr* > 1.

I. INTRODUCTION

Understanding the complex dynamic behavior of particle transportation in shear flows is important in a variety of industrial and biological applications [1–6]. Recently, inertial migration of particle suspensions has prompted great potential in microfluidic applications, because of the increased control and precision in manipulation and separation of microparticles [7–9]. Segré and Silberberg first observed experimentally the tubular pinch effect in the pipe flow of neutrally buoyant particle suspensions [10], where particles migrate across streamlines due to inertial effects and are equilibrated at a radial position around 0.6 radius of the pipe. This counterintuitive observation motivated a flurry of subsequent studies to explore the underlying physics of such a fascinating phenomenon [11–20], as there was no theoretical explanation at the time when it was discovered. It was well recognized that the equilibrium position of a particle in a shear flow was determined

---

*Corresponding authors: liuwenwei@ipe.ac.cn; c.y.wu@surrey.ac.uk

by the synthetic effects of several forces, including a lubrication force close to the wall boundary, a lift force due to slip velocity (Saffman lift force), a lift force due to particle rotation (Magnus lift force), and a lift force caused by the curvature of the fluid velocity profile (only in Poiseuille flow) [16]. The dominating lateral forces on the particle were derived theoretically with the technique of matched asymptotic expansions [12,14,17,19,20].

The majority of previous studies on inertial migration in shear flows are confined to the isothermal condition. However, there are plenty of examples that such multiphase flows are frequently accompanied by phase change, reaction, and heat transfer [21–27], which are not well understood theoretically. The most challenging problems stem from several mesoscopic features: (1) the coupling of heat and mass transfer between fluid flow and the moving interfaces; (2) the complicated interaction and the heat transfer among neighboring particles [23]. Over the past two decades, a large number of studies investigated the effects of mixed convection on the particle's motion [23,28–34]. Nevertheless, much attention was paid to the particle settling behavior in the presence of thermal convection, e.g., the settling trajectory with different Grashof numbers [23,28], the drag coefficient of a settling particle [29], and the effects of temperature boundary conditions [30,31], as well as the drafting-kissing-tumbling phenomenon of two cold particles [32]. Very few studies were performed to explore the thermal effects on inertial migration of a particle in shear flows. To our best knowledge, the only works were conducted by Hu and Guo [33] and Safa *et al.* [34] recently. Hu and Guo [33] numerically investigated inertial migration of a cold neutrally buoyant particle in a planar Poiseuille flow and found that the particle's equilibrium position changed from above the centerline to below the centerline as the Grashof number reached a critical value. Safa *et al.* [34] investigated the lateral migration of a cold particle in a Couette flow and discovered that the equilibrium position of the particle moves toward the bottom wall with the increase of the Grashof number. Their works are confined to only neutrally buoyant particles and a very narrow range of parameters. A comprehensive understanding of such migration behavior with thermal effects still deserves further exploration.

Undoubtedly, the thermal effects play a significant role in determining the particle's lateral migration position. However, the physics underlying inertial migration in nonisothermal shear flows is still not well understood. The motivations of the present work are not only exploring the heat transfer in sheared particle suspensions [35], but also attempting to seek the potential application in a thermal energy storage system with fluidized bed and suspensions [36–38], where both the fluid and the particles are heated by solar energy. Therefore, in this work we start with the inertial migration of a particle in a simple shear flow in the presence of thermal convection, which is investigated numerically using a double-population lattice Boltzmann method (LBM). Different from the previous studies, the main focus of the present study is on non-neutrally buoyant particles with solid-fluid density ratios in the range of 0.98–1.02, for which the particle's equilibrium position is determined by not only the hydrodynamics, but also the thermal effects and the buoyancy.

II. NUMERICAL METHOD

A. Double-population lattice Boltzmann method

In this study, the fluid field and temperature field are modeled using the double-population lattice Boltzmann method, in which the single relaxation time model [Bhatnagar-Gross-Krook (BGK) approximation] is employed in the relaxation collision operator [39,40]. The viscous heat dissipation and compression work carried out by the pressure are not considered, so that the temperature field is treated as a passive scalar and advected by the fluid flow. The governing lattice Boltzmann equations are given, respectively, as [41,42]

$$f_i(\mathbf{x} + \mathbf{e}_i \Delta t, t + \Delta t) - f_i(\mathbf{x}, t) = -\frac{1}{\tau_f} \big[f_i(\mathbf{x}, t) - f_i^{\text{eq}}(\mathbf{x}, t) \big] + F_i \Delta t, \tag{1}$$

$$g_i(\mathbf{x} + \mathbf{e}_i \Delta t, t + \Delta t) - g_i(\mathbf{x}, t) = -\frac{1}{\tau_g} \big[g_i(\mathbf{x}, t) - g_i^{\text{eq}}(\mathbf{x}, t) \big] + S_i \Delta t, \tag{2}$$

where τ_f and τ_g are the dimensionless relaxation parameters for the fluid and temperature fields, respectively. $f_i(\mathbf{x}, t)$ and $g_i(\mathbf{x}, t)$ represent the distribution functions for fluid and temperature at position $\mathbf{x}$ and time t, respectively. F_i and S_i denote the external body force and heat source term, respectively. Δt is the time step, which is usually set as 1 in the LBM lattice unit. $f_i^{\text{eq}}(\mathbf{x}, t)$ and $g_i^{\text{eq}}(\mathbf{x}, t)$ are the distribution functions at the equilibrium state, and are defined as

$$f_i^{\text{eq}} = \rho_f \omega_i \left[1 + \frac{\mathbf{e}_i \cdot \mathbf{u}}{c_s^2} + \frac{(\mathbf{e}_i \cdot \mathbf{u})^2}{2c_s^4} - \frac{u^2}{2c_s^2} \right], \tag{3}$$

$$g_i^{\text{eq}} = T \omega_i \left[1 + \frac{\mathbf{e}_i \cdot \mathbf{u}}{c_s^2} \right], \tag{4}$$

where $c_s = 1/\sqrt{3}$ is the lattice sound speed. ρ_f, $\mathbf{u}$, and T are the macroscopic fluid density, velocity, and temperature, respectively. ω_i is the weight coefficient decided by the lattice speed model. In this work, the D2Q9 lattice speed model is employed so that the discrete velocity vectors $\mathbf{e}_i$ are defined as

$$\mathbf{e}_i = \begin{cases} (0, 0), & i = 0 \\ \left(\cos \frac{i\pi - \pi}{2}, \ \sin \frac{i\pi - \pi}{2} \right), & i = 1, 2, 3, 4 \\ \left(\cos \frac{2i\pi - 9\pi}{4}, \ \sin \frac{2i\pi - 9\pi}{4} \right), & i = 5, 6, 7, 8 \end{cases} \tag{5}$$

Correspondingly, the weight coefficient ω_i for the D2Q9 model is given as

$$\omega_0 = \tfrac{4}{9}, \quad \omega_{1,2,3,4} = \tfrac{1}{9}, \quad \omega_{5,6,7,8} = \tfrac{1}{36}. \tag{6}$$

The macroscopic fluid quantities are determined by the microscopic distribution functions via the following equations,

$$\rho_f = \sum_i f_i, \tag{7}$$

$$\rho_f \mathbf{u} = \sum_i f_i \mathbf{e}_i + \frac{\Delta t}{2} \mathbf{F}, \tag{8}$$

$$T = \sum_i g_i, \tag{9}$$

where $\mathbf{F}$ represents the macroscopic body force. The external body force term F_i in Eq. (1) is explicitly defined with the following force scheme [43]:

$$F_i = \left(1 - \frac{1}{2\tau_f} \right) \omega_i \left[\frac{\mathbf{e}_i - \mathbf{u}}{c_s^2} + \frac{(\mathbf{e}_i \cdot \mathbf{u})}{c_s^4} \mathbf{e}_i \right] \cdot \mathbf{F}. \tag{10}$$

To couple the fluid flow with the temperature field, the Boussinesq approximation is adopted and expressed as

$$\rho_f = \rho_0 [1 - \beta(T - T_{\text{ref}})], \tag{11}$$

where ρ_0 is the fluid density at the reference temperature T_{ref}, and β is the thermal expansion coefficient of the fluid. Hence an external buoyancy force is exerted on the fluid due to the temperature difference,

$$\mathbf{F}_B = -\rho_0 \mathbf{g} \beta(T - T_{\text{ref}}), \tag{12}$$

where $\mathbf{g}$ is the gravitational acceleration. In the current work, only the thermal convection between the particle and the wall is considered, so that the heat source term S_i in Eq. (2) is assumed to be zero.

The macroscopic continuum equation and momentum equation, as well as the energy equation can be recovered from the microscopic lattice Boltzmann equations, i.e., Eqs. (1) and (2), using the Chapman-Enskog multiscale expansion [44] as follows

$$\nabla \cdot \mathbf{u} = 0, \tag{13}$$

$$\rho_f \frac{\partial \mathbf{u}}{\partial t} + \rho_f (\mathbf{u} \cdot \nabla) \mathbf{u} = -\nabla p + \mu \nabla^2 \mathbf{u} + \mathbf{F}, \tag{14}$$

$$\frac{\partial T}{\partial t} + \mathbf{u} \cdot \nabla T = \alpha \nabla^2 T, \tag{15}$$

where p is the fluid pressure, which is determined by $p = c_s{}^2 \rho_f$, μ is the fluid dynamic viscosity, and α is the thermal diffusion coefficient. The fluid kinematic viscosity ν and thermal diffusivity α can be obtained with the relaxation parameters τ_f and τ_g, respectively, using the Chapman-Enskog expansion,

$$\nu = \frac{2\tau_f - 1}{6}, \tag{16}$$

$$\alpha = \frac{2\tau_g - 1}{6}. \tag{17}$$

B. Fluid-solid coupling

The fluid-solid coupling plays an important role in determining the hydrodynamic interactions between the fluid and the particle. In this work, an interpolated bounce-back technique is employed to account for the fluid-solid interaction, which is proved to be of second-order accuracy [45,46]. When a solid particle moves in a fluid domain meshed with discrete lattice grids, its solid boundary is usually not located exactly on any lattice node. Assume that the solid boundary lies between a fluid node $\mathbf{x}_f$ and a solid node $\mathbf{x}_s$ at time t, where the exact position of the solid boundary is denoted as $\mathbf{x}_b$; the relative location of the solid boundary is described with a weighting parameter,

$$q = |\mathbf{x}_f - \mathbf{x}_b| / |\mathbf{x}_f - \mathbf{x}_s|. \tag{18}$$

The undetermined distribution function $f_{-i}(\mathbf{x}_f, t + \Delta t)$ bounced back from the solid boundary $\mathbf{x}_b$ is computed using the following three steps, where $-i$ denotes the direction from the solid node $\mathbf{x}_s$ to the fluid node $\mathbf{x}_f$.

Firstly, using the existing distribution functions $f_i(\mathbf{x}_f, t)$ and $f_i(\mathbf{x}_{ff}, t)$ at the nearest fluid nodes $\mathbf{x}_f$ and $\mathbf{x}_{ff}$ the distribution function at the solid boundary $f_i(\mathbf{x}_b, t + \Delta t)$ is calculated with a first-order interpolation,

$$f_i(\mathbf{x}_b, t + \Delta t) = q f_i(\mathbf{x}_f, t) + (1 - q) f_i(\mathbf{x}_{ff}, t). \tag{19}$$

Secondly, an instantaneous bounce-back operation at the solid boundary $\mathbf{x}_b$ gives

$$f_{-i}(\mathbf{x}_b, t + \Delta t) = f_i(\mathbf{x}_b, t + \Delta t) - 2\omega_i \rho \mathbf{u}_b \cdot \mathbf{e}_i, \tag{20}$$

where $\mathbf{u}_b$ is the velocity of the solid boundary.

Finally, the unknown distribution function $f_{-i}(\mathbf{x}_f, t + \Delta t)$ is interpolated with the newly obtained $f_{-i}(\mathbf{x}_b, t + \Delta t)$ and existing distribution function $f_{-i}(\mathbf{x}_{ff}, t + \Delta t)$,

$$f_{-i}(\mathbf{x}_f, t + \Delta t) = \frac{1}{1+q} f_{-i}(\mathbf{x}_b, t + \Delta t) + \frac{q}{1+q} f_{-i}(\mathbf{x}_{ff}, t + \Delta t). \tag{21}$$

Note that second-order interpolation is also applicable, which requires the distribution function from further fluid node $\mathbf{x}_{fff}$.

The hydrodynamic force on the particle at the solid boundary $\mathbf{x}_b$ is computed using the momentum exchange method with a Galilean invariance to reduce the unphysical numerical error [46], which is evaluated as

$$\mathbf{F}_i = (\mathbf{e}_i - \mathbf{u}_b)f_i^+(\mathbf{x}_f, t) - (\mathbf{e}_{-i} - \mathbf{u}_b)f_{-i}(\mathbf{x}_f, t + \Delta t). \tag{22}$$

Then the total hydrodynamic force and torque are calculated by summing up all the contributions from every lattice direction and every nearest fluid node,

$$\mathbf{F}_f = \sum_{\text{all } \mathbf{x}_f} \sum_i \mathbf{F}_i, \tag{23}$$

$$\mathbf{M}_f = \sum_{\text{all } \mathbf{x}_f} \sum_i (\mathbf{x}_b - \mathbf{x}_c) \times \mathbf{F}_i. \tag{24}$$

For the boundary conditions of temperature field, only the Dirichlet boundary condition, i.e., the constant temperature boundary, is considered. A general bounce-back scheme for the concentration boundary condition is applied in the current study [47], which yields

$$g_{-i}(\mathbf{x}_f, t + \Delta t) = -g_i^+(\mathbf{x}_f, t) + 2\omega_i T_b \times [1.0 + 4.5(\mathbf{e}_i \cdot \mathbf{u}_b)^2 - 1.5|\mathbf{u}_b|^2], \tag{25}$$

where T_b is the temperature at the interface and $g_i^+(\mathbf{x}_f, t + \Delta t)$ is the postcollision distribution function at the fluid node $\mathbf{x}_f$.

C. Particle's motion

The translational and rotational motions of solid particles are governed by Newton's equations of motion,

$$m \frac{d\mathbf{u}_p}{dt} = \mathbf{F}_f + \mathbf{G}, \tag{26}$$

$$I \frac{d\mathbf{\Omega}_p}{dt} = \mathbf{M}_f, \tag{27}$$

where $\mathbf{u}_p$ and $\mathbf{\Omega}_p$ are the transitional and rotational velocities of the particle, respectively. m is the particle mass and I is the moment of inertia. $\mathbf{F}_f$ and $\mathbf{M}_f$ represent the fluid force and the torque exerting on the particle, respectively. $\mathbf{G}$ is the gravity. Given that only one particle is considered in the current work, the interparticle collision will not come into effect. To account for the particle-wall interaction, the lubrication effect between the particle and the wall is carefully considered, in order to prevent the particle from touching the wall due to the interstitial fluid pressure. An analytical representation is employed to describe the lubrication force $\mathbf{F}_{\text{lub}}$ [48],

$$\mathbf{F}_{\text{lub}} = -6\pi \mu r^2 \mathbf{v}_R(h)\left(\frac{1}{h} - \frac{1}{h_{\text{crit}}}\right), \tag{28}$$

where $\mathbf{v}_R(h)$ is the relative velocity between the particle and the wall at the gap h, r is the particle radius, and h_{crit} is the critical gap distance to trigger the lubrication correction, which is set as one lattice grid $h_{\text{crit}} = 1$ in the current work. When the gap between the particle and the wall is larger than h_{crit}, the lubrication force is not computed. Therefore, the total hydrodynamic force on the particle is given as

$$\mathbf{F}_{\text{hydro}} = \begin{cases} \mathbf{F}_f, & h \geqslant h_{\text{crit}} \\ \mathbf{F}_f + \mathbf{F}_{\text{lub}}, & h < h_{\text{crit}} \end{cases}, \tag{29}$$
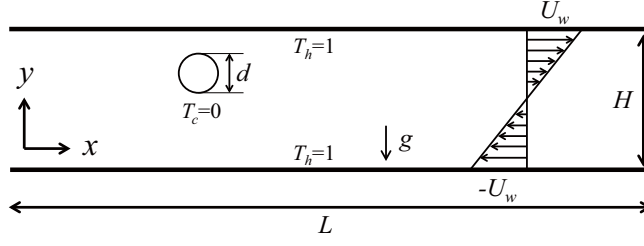
FIG. 1. Schematic of the model setup.

where $\mathbf{F}_f$ is the fluid force calculated from the LBM [see Eq. (23)]. More detailed discussions on the LBM–discrete element method (DEM), including model validation and applications, can be found in our recent paper [49–51].

D. Simulation setup

As depicted in Fig. 1, a single particle with diameter $d = 10$ is initially suspended in a two-dimensional channel with length L and height H. Periodic boundary conditions are considered at the inlet and outlet of the domain. The top and bottom walls move with constant velocities U_w and $-U_w$, respectively, which creates a simple shear flow with a constant shear rate $\gamma = 2U_w/H$. For the lattice dimensions, the length of the channel is set as $L = 500$, which is sufficient to eliminate the periodic effect, while the height is fixed at $H = 100$. To explore the effect of buoyancy, the particle's mass density is varied between 0.98 and 1.02 without being equal to 1. The effect of thermal convection is imposed by applying the Dirichlet boundary conditions on the particle surface as well as the top and bottom walls. The particle surface is kept at a cold temperature, $T_c = 0$, while the top and bottom walls are set with a hot temperature, $T_h = 1$. The initial temperature of the fluid is the same as that of the wall. The reference temperature in this study is selected as $T_h = 1$, and the fluid density at $T_h = 1$ is defined as the reference value to determine the density ratio.

The dimensionless control parameters for this problem include the dimensionless density ratio σ, the Prandtl number Pr, the channel Reynolds number Re, and the Grashof number Gr, which are defined as

$$\sigma = \frac{|\rho_p - \rho_f|}{\rho_f}, \tag{30}$$

$$\mathrm{Pr} = \frac{\nu}{\alpha}, \tag{31}$$

$$\mathrm{Re} = \frac{2U_w H}{\nu}, \tag{32}$$

$$\mathrm{Gr} = \frac{g\beta(T_h - T_c)d^3}{\nu^2}. \tag{33}$$

Note that the particle Reynolds number based on the shear rate is also defined, $\mathrm{Re}_p = \frac{\gamma d^2}{\nu}$, which is related to the channel Reynolds number via $\mathrm{Re}_p = \mathrm{Re}(\frac{d}{H})^2$. Since the particle size used in this work is a fixed value, the two Reynolds number can be easily converted to each other through a constant factor. The Prandtl number is fixed at $\mathrm{Pr} = 0.7$, and the channel Reynolds number is in the range of $\mathrm{Re} = 20-500$. Hence the particle Reynolds number ranges from 0.2 to 5, which is in the laminar flow regime. Table I gives a summarization of the major computational parameters used in the simulations.

TABLE I. A list of simulation parameters.

Physical parameters	Lattice value
Channel length (L)	500
Channel height (H)	100
Fluid density (ρ_f)	1
Fluid kinematic viscosity (ν)	0.05
Wall velocity (U_w)	0.005–0.125
Particle diameter (d)	10
Particle mass density (ρ_p)	0.98–1.02
Prandtl number (Pr)	0.7
Channel Reynolds number (Re)	20–500
Grashof number (Gr)	0–55

III. NUMERICAL VALIDATION

The numerical method is validated through two benchmark tests. One is the inertial migration of a neutrally buoyant particle in a simple shear flow under the isothermal condition, and the other is the sedimentation of a cold particle in hot fluid under gravity. The two validations ensure that the well-known lateral migration phenomenon can be reproduced and the heat convection between particle and fluid is computed correctly.

A. Inertial migration of a neutrally buoyant particle in simple shear flow under isothermal condition

The setup of the validation is the same as illustrated in Fig. 1, except that the thermal convection is not considered. A particle with diameter of $d = 25$ is initially released at two symmetrical starting positions $y_0/H = 0.25$ and $y_0/H = 0.75$. The channel Reynolds number is fixed at Re $= 40$. All the parameters are identical to those used in [16].

Under the isothermal condition, the particle will migrate toward the centerline of the channel, which is the only equilibrium position for a simple shear flow. Figure 2 shows a quantitative comparison of the particle's lateral trajectory obtained in our numerical simulation with the results in [16]. Obviously, excellent agreement is reached between our numerical results and the literature.
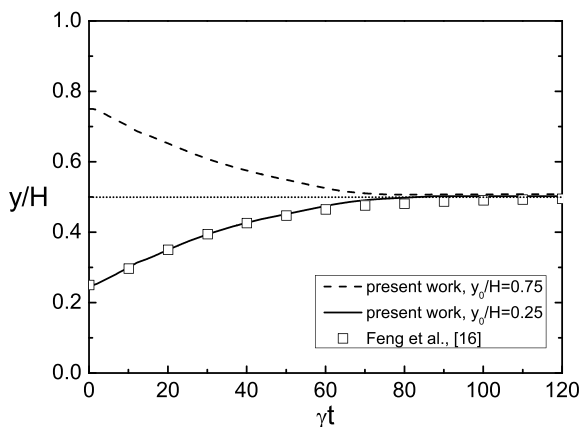

FIG. 2. Particle's lateral trajectory in a simple shear flow under isothermal condition. The open square denotes the results from Feng *et al.* [16].
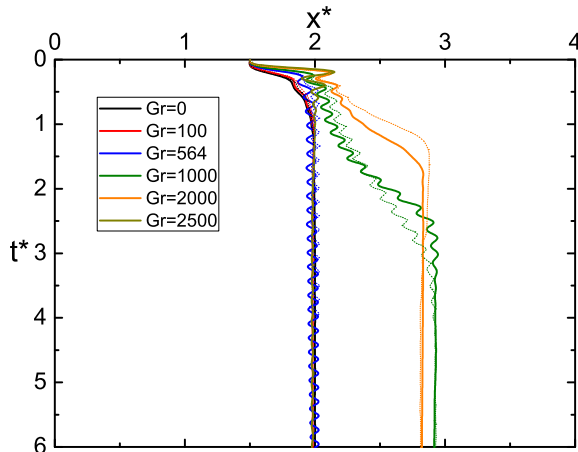
FIG. 3. Time evolution of the particle's horizontal position for different particle Grashof numbers. The normalized values are defined as $x^* = x/W$ and $t^* = t\nu/d^2$. The solid lines denote the results of the present work, while the dotted lines are results from [33].

Therefore, it is believed that our numerical model is able to predict the hydrodynamics and reproduce the inertial migration in simple shear flow.

B. Sedimentation of a cold particle in a hot fluid

Sedimentation of a cold particle in a hot fluid bounded by two vertical walls is a well-validated benchmark test for thermal fluid-particle problems and has been revisited by many scholars [23,30,32,33]. It is well accepted that the settling trajectory of a single particle remarkably depends on the particle Grashof number, $\mathrm{Gr}_p = g\beta\Delta T d^3/\nu^2$, where six different regimes of settling behavior are identified. Particularly, when $810 < \mathrm{Gr}_p < 2150$, the particle settles vertically at a horizontal position away from the centerline [23], which is the only settling position at the equilibrium state under the isothermal condition.

To reproduce the interesting settling phenomenon, several typical Grashof numbers are selected from different regimes. The computational domain with size of $W \times H = 100 \times 8000$ is bounded by four no-slip walls, where the left and right walls are imposed with a hot temperature $T_w = 1$, while the top and bottom walls are adiabatic, i.e., $dT/dy = 0$. The initial fluid temperature is also $T_w = 1$, and the temperature of the particle surface is fixed at $T_p = 0$. The particle with diameter of $d = 25$ is initially released at a position $d/2$ away from the centerline and $5d/2$ away from the top wall. The density ratio of the particle to the fluid is $\rho_p/\rho_f = 1.00232$. The height of the channel is sufficiently long, so that the particle can reach the steady state of settling before touching the bottom wall. The reference particle Reynolds number is fixed at $\mathrm{Re}_p = U_{\mathrm{ref}}d/\nu = 40.5$, which is the same as used in the literature [23,28], with U_{ref} being the reference velocity $U_{\mathrm{ref}} = \sqrt{\pi d(\rho_p/\rho_f - 1)g/2}$. The relaxation parameter is set as $\tau_f = 0.65$ and the Prandtl number is fixed at $\mathrm{Pr} = 0.7$.

Figure 3 shows the time evolution of the particle's horizontal position for different particle Grashof numbers, where the numerical results from [33] are also included for comparison. It is clear that our results are in qualitative agreement with the literature. A further quantitative comparison of the equilibrium positions at $\mathrm{Gr} = 1000$ and $\mathrm{Gr} = 2000$ are listed in Table II. It can be seen that excellent agreement is realized between our numerical results and the literature, which demonstrates the applicability and validity of our numerical approach.

TABLE II. Equilibrium positions of the particle at Gr = 1000 and Gr = 2000.

Gr	Present work	Reference [28]	Reference [33]
1000	2.92	2.89	2.91
2000	2.76	2.74	2.76

IV. RESULTS AND DISCUSSIONS

A. Lattice grid independency

The independence of the lattice resolution is first examined by using different grids with the same Reynolds number and Grashof number. The grid setup is set as $20d \times 10d$ and three different size resolutions $d = 10, 16, 20$ are employed. The Reynolds number is fixed at Re = 100 and the Grashof number is Gr = 1. For convenience, the particle is neutrally buoyant in the grid independency test and its initial position is fixed at $y_0/H = 0.6$. Figure 4 shows the particle lateral trajectory for different grid setups. Obviously, there is no considerable difference in the equilibrium position for all lattice grids considered. Hence, the lattice grid of $d = 10$ is believed to be sufficient to obtain reliable results.

When a particle is released from rest at a certain height in the shear flow, it is expected that the particle will settle to the bottom of the channel when $\rho_p > \rho_f$, and rise to the top when $\rho_p < \rho_f$, in the absence of shear flow. However, the shear flow produces a lift force on the particle, which is toward the centerline, according to previous studies [16]. Thus, for a slightly non-neutrally buoyant particle, it can be suspended again in the channel when the lift force is large enough to overcome the gravitational force (buoyancy). Nevertheless, it was also reported that the presence of thermal convection creates an additional lift force on the particle, which is always toward the bottom of the channel when the particle is cold and the fluid is hot [33,34,52]. As a result, it is apparent that the migration behavior of a non-neutrally buoyant particle depends on whether its density is larger or smaller than the fluid, which will thus be discussed separately below.

B. Particles with $\rho_p > \rho_f$

We start with the migration of a particle that is heavier than the fluid, under the isothermal condition. Figure 5(a) shows the time evolution of the lateral position of the particle with various
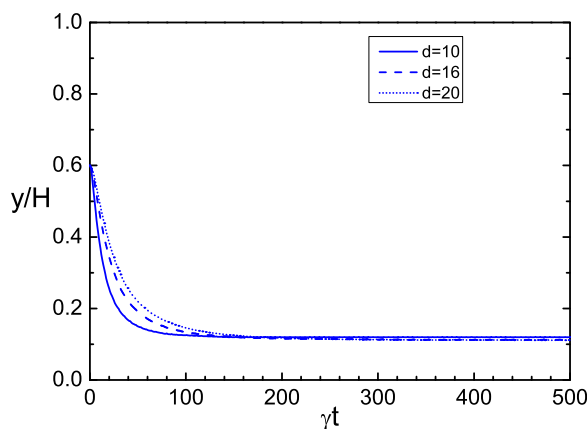

FIG. 4. Particle lateral position as a function of time for different lattice grids with the same Reynolds number Re = 100 and Grashof number Gr = 1.
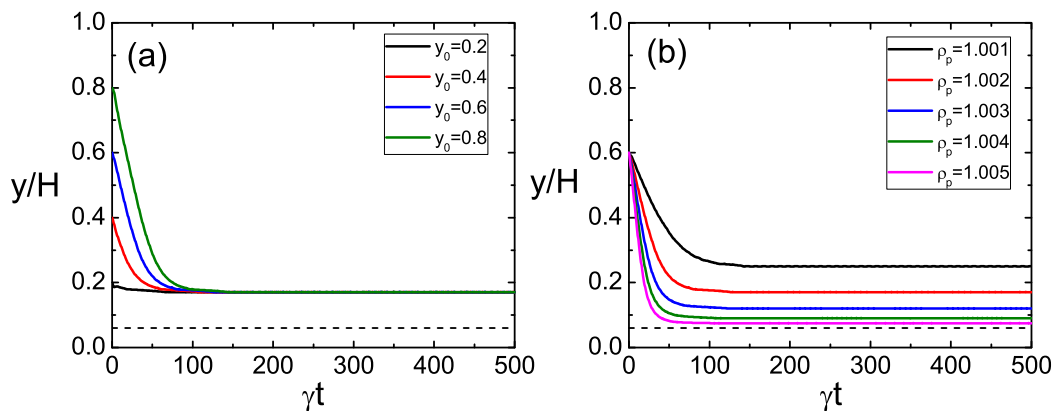
FIG. 5. Time evolution of the lateral position of particles with (a) different initial positions with the same $\rho_p = 1.002$, and (b) different particle densities. The Reynolds number is fixed at Re = 100 and the Grashof number is Gr = 0. The dashed lines represent the bottom of the channel.

initial positions. It can be seen that the particle ends up at the same equilibrium position with the same Reynolds number and density, which implies that the final equilibrium position is independent of the initial position. Therefore, the initial releasing position of the particle is fixed at $y_0/H = 0.6$ in the following discussions, if not particularly mentioned. Figure 5(b) shows the trajectory of the particle with different densities and the same Reynolds number. It is clear that heavier particle settles closer to the bottom of the channel, due to the larger gravitational force. The equilibrium positions of the particle as a function of the Reynolds number are further analyzed and shown in Fig. 6. It can be observed that the particle reaches the bottom of the channel, which corresponds to a dimensionless height of $y/H = 0.06$, at a relatively low Reynolds number. With the increase of Reynolds number, the particle becomes suspended again in the channel at some critical points and lifts to a higher equilibrium position when Re is further increased. Moreover, Fig. 6 also reveals that the critical Reynolds number increases with the increase of particle density. Hence it is of interest to identify the conditions when a particle settles to the bottom or remains suspended at an equilibrium position.
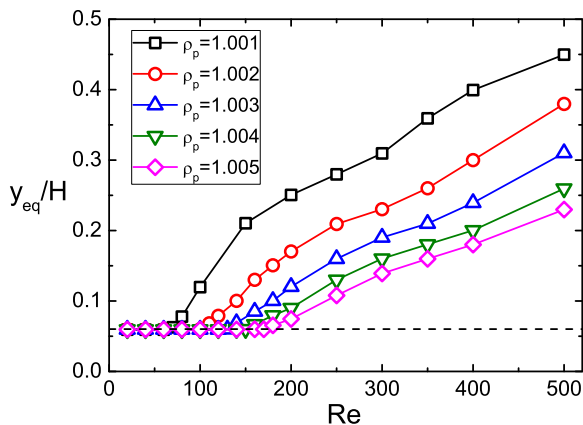

FIG. 6. Equilibrium positions of the particle as a function of the Reynolds number for different densities. The dashed line represents the bottom of the channel.
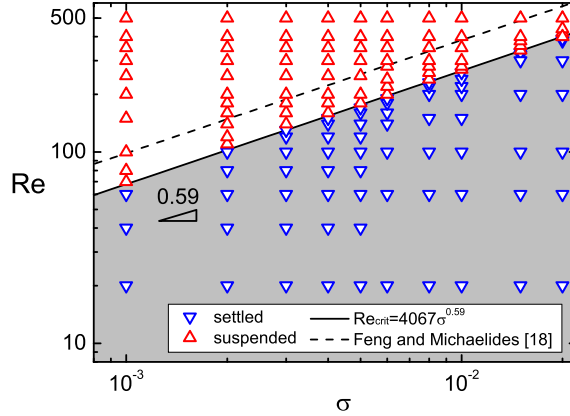
FIG. 7. The regime map showing whether a particle is settled or suspended in terms of the dimensionless density ratio and Reynolds number. The dashed line represents the results from Feng and Michaelides [18].

Following the work of Feng and Michaelides [18], more simulations were carried out with a wider range of the parameters, i.e., Re $= 20-500$ and $\sigma = 0.001-0.02$. To assess whether a particle settles at the bottom or remains suspended, a critical distance from the lower tip of the particle to the bottom of the channel is defined as one lattice unit in the current study, which is equivalent to a dimensionless height of $y/H = 0.01$. Thus, a particle with an equilibrium position $y_{eq}/H \leqslant 0.06$ is regarded as settled, while it is suspended if $y_{eq}/H > 0.06$. In Fig. 7, whether a particle is settled or suspended is illustrated for a wide range of the dimensionless density ratio σ and Re considered. Two distinctive regions are identified and the boundary curve can be well described with a power law

$$\mathrm{Re}_{\mathrm{crit,Gr=0}} = a\sigma^{b},$$ (34)

where $a = 4067$ and $b = 0.59$. It is noted that the exponent $b = 0.59$ in the above correlation function is in excellent agreement with the result reported by Feng and Michaelides [18] that is also superimposed in Fig. 7 using the dashed line. The overestimation of the critical Reynolds number in Feng and Michaelides' work might be attributed to the different model setups in the simulation.

Furthermore, a new dimensionless parameter can be deduced from Eq. (34),

$$\lambda_H = \frac{\mathrm{Re}}{\mathrm{Re}_{\mathrm{crit,Gr=0}}} = \frac{\mathrm{Re}}{4067\sigma^{0.59}},$$ (35)

which can be treated as a relative strength between the lift force represented by the Reynolds number, and the driving force of settling denoted by the density difference. With this dimensionless parameter, the equilibrium positions of all the simulation conditions are quantified in a unified form, and the results are shown in Fig. 8. It can be seen from Fig. 8 that the equilibrium positions for a particle with different Reynolds numbers and densities coalescence into a single master curve and can be well depicted with the new parameter λ_H. When $\lambda_H < 1$ the particle settles at the bottom of the channel. When $\lambda_H > 1$, the equilibrium position of the particle increases consistently with the increase of λ_H, which is well described by a logarithmic function,

$$\frac{y_{eq}}{H} = c_1 \ln(\lambda_H) - c_2,$$ (36)

where the fitting parameters are $c_1 = 0.184$ and $c_2 = 0.051$ in the current study.

However, the above discussions are only confined to isothermal condition, where the influence of thermal convection is not included. Then simulations with different Grashof numbers were performed to explore the effect of thermal convection on the particle migration. The equilibrium
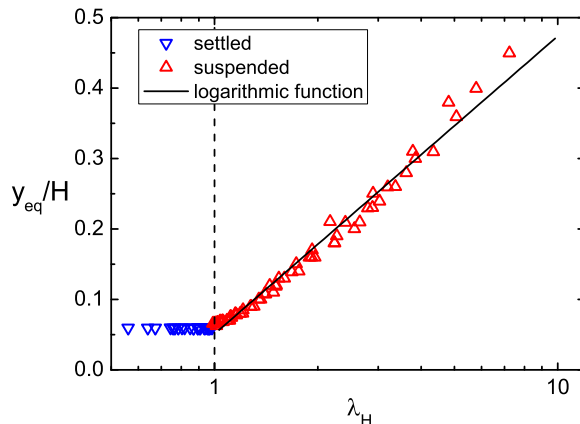
FIG. 8. Equilibrium positions as a function of λ_H.

positions as a function of the Grashof number for different densities and Reynolds numbers are shown in Fig. 9. It is observed that the equilibrium position decreases with the increase of the Grashof number, when the particle is suspended at Gr = 0. However, when the particle already settles at the bottom of the channel at Gr = 0, thermal convection has little effect on the equilibrium position. For example, the equilibrium position of the particle with $\rho_p = 1.002-1.005$ and Re = 100 stays at the bottom of the channel for all the Grashof numbers, while the equilibrium position of the particle with $\rho_p = 1.001$ and Re = 100 drops from $y_{eq}/H = 0.12$ to $y_{eq}/H = 0.06$ when Gr is increased from 0 to 40. These observations confirm that the thermal convection facilitates the settling of the particle. Furthermore, it is interesting that the equilibrium position seems to reach a stable value when the Grashof number is increased to a very large value, which appears not necessarily to be the bottom of the channel ($y_{eq}/H = 0.06$). Hence this stable lateral position is defined as an asymptotic equilibrium position of the particle at the infinite Grashof number limit (Gr $\rightarrow \infty$). As can be seen from Figs. 9(b) and 9(c), the asymptotic equilibrium position moves away from the bottom of the channel with the increase of Reynolds number, and seems to be slightly different for different particle densities. As a result, it is anticipated that there are still two distinguished regions, i.e., settled and suspended, for the particle migration behavior at the infinite Grashof number limit, which also depend on the Reynolds number and the particle density.

Similarly, a regime map can be constructed in terms of Re and σ to indicate when a particle is settled or suspended at Gr $\rightarrow \infty$, and the result is displayed in Fig. 10. Note that the equilibrium position at Gr = 30 is used as a representative value at the infinite Grashof number limit. It is observed from Fig. 10 that, comparing to the isothermal regime map (see Fig. 7), the region of
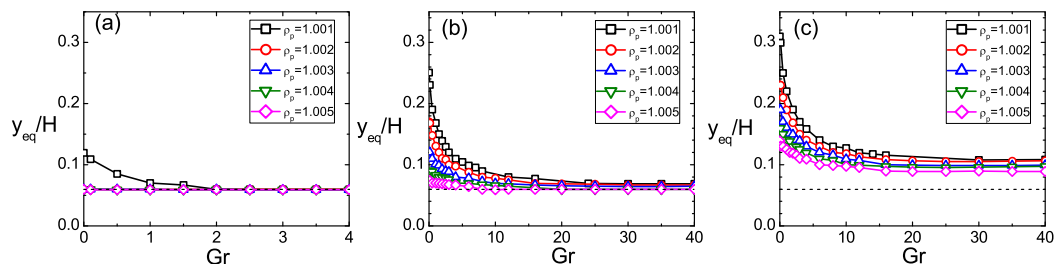
FIG. 9. Equilibrium position as a function of Grashof number for different particle densities and Reynolds numbers: (a) Re = 100, (b) Re = 200, and (c) Re = 300. The dashed line represents the bottom of the channel.

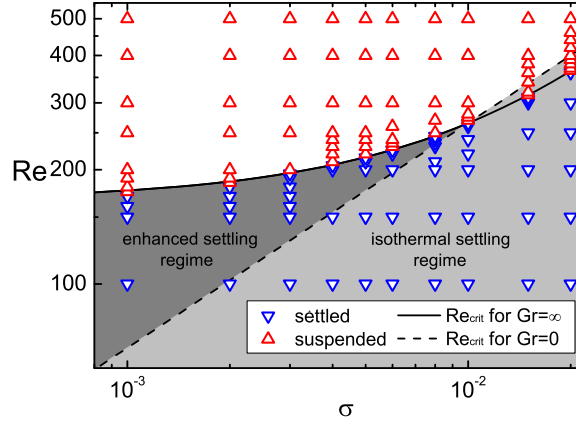FIG. 10. A regime map showing whether a particle is settled or suspended in terms of Re and σ at Gr $= 30$.

settled particles is enlarged, which is denoted by the dark gray area. In this enlarged region, a particle that originally remains suspended at Gr $= 0$ settles to the bottom of the channel at Gr $\rightarrow \infty$, implying that a higher Re is needed to lift the particle to be suspended again in the presence of thermal convection. Hence, we termed this area as a thermal convection enhanced settling regime. Furthermore, the critical Reynolds number, i.e., the boundary curve between settled and suspended regions, does not follow the power law given in Eq. (34), but can be described with a linear function,

$$\mathrm{Re}_{\mathrm{crit},\mathrm{Gr}\rightarrow\infty} = c_3\sigma + c_4, \tag{37}$$

where the fitting parameters are $c_3 = 9873.6$ and $c_4 = 166.4$ in the current study. Note that the power law in Eq. (34) is also incorporated in Fig. 10 for comparison. It can be seen that the linear function lies above the power law in the range $\sigma = 0-0.01$, and almost collapses with the power law when $\sigma > 0.01$, which implies a nonlinear dependence of the thermal convection enhanced settling on the particle density. For example, the critical Reynolds number is increased from $\mathrm{Re}_{\mathrm{crit}} = 65$ at Gr $= 0$ to $\mathrm{Re}_{\mathrm{crit}} = 173$ at Gr $\rightarrow \infty$ when $\sigma = 0.001$, while it is almost the same for $\sigma = 0.01$; i.e., $\mathrm{Re}_{\mathrm{crit}} = 265$ at Gr $= 0$ and $\mathrm{Re}_{\mathrm{crit}} = 268$ at Gr $\rightarrow \infty$. Hence it can be inferred that the thermal convection imposes greater influences on the settling of a relatively lighter particle ($\sigma < 0.01$). However, when $\sigma > 0.01$, the critical Reynolds number is almost the same for Gr $= 0$ and Gr $\rightarrow \infty$, which indicates that thermal convection has little effect on the migration behavior of the particle.

It was previously reported that the introduction of thermal convection produces an additional downward lift force on a cold particle in a hot fluid [33,34,52], which increases with the increase of the Grashof number. Thus, the lift force caused by thermal convection is in the same direction as the gravitational force, as depicted in Fig. 11(a), which enhances the settling of the particle. The other lateral forces, including the wall repulsion, the Saffman force due to shear flow, and the Magnus force due to particle rotation [16], are all against these two driving forces. The magnitude of the inertial lift force in a simple shear flow is scaled as $F_L \propto \rho_f U^2 d^4/H^2$ based on the asymptotic expansion technique [12,17], where U denotes the mean fluid velocity. Considering that the sizes of the channel and the particle are constant in the current study, the inertial lift force only depends on the fluid velocity, which can be related to the Reynolds number. The gravitational force is determined by the dimensionless density ratio. Therefore, the equilibrium position of a particle that is heavier than the fluid is a result of the complicated competition between the inertial lift force and the synergistic effect of both gravitational force and thermal convection, which are further reduced to three dominating dimensionless parameters, i.e., Re, σ, and Gr.
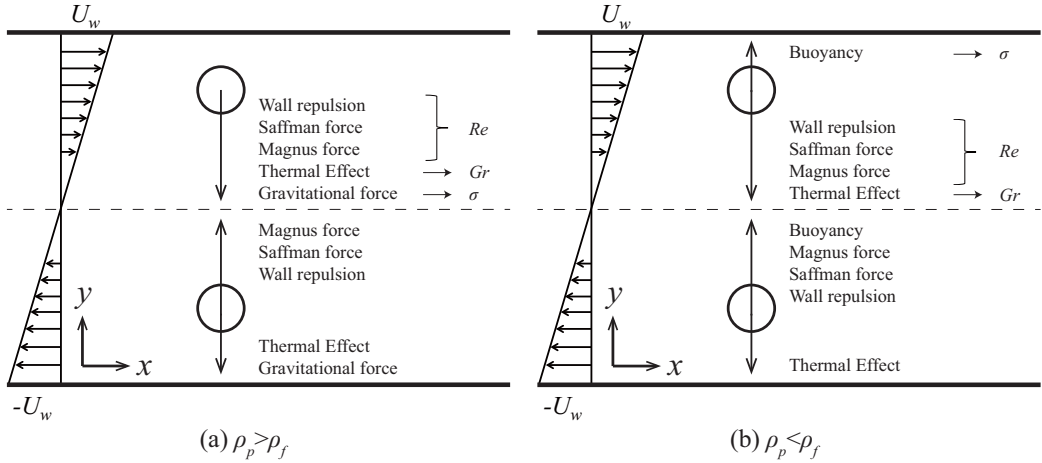
FIG. 11. Lateral forces on a particle that is (a) heavier than the fluid and (b) lighter than the fluid in the simple shear flow.

To further examine the various forces exerted on the particle, the lateral trajectory and the slip velocity, as well as the fluid pressure distribution, are analyzed with more details. First, the effect of Magnus force is revealed by turning off the particle rotation. As shown in Fig. 12(a), it can be seen that the particle rotation seems to have limited impact on the equilibrium position, where the particle without rotation is equilibrated at a slightly lower place. This is because the Magnus force is always toward the centerline when the particle is in the bottom half of the channel due to a clockwise rotation. Once it is switched off, the total upward force decreases, so that a new lower equilibrium position must be met. Figure 12(b) shows the particle's slip velocity as a function of time, which is defined as the difference between the particle velocity and the undisturbed fluid velocity at the center of the particle. It is found out that the particle's slip velocity is almost zero for the isothermal case, while it increases to larger positive value as the Grashof number increases, which indicates that the particle always leads the fluid in the presence of thermal convection. Hence, an upward Saffman lift force toward the centerline is produced due to a larger relative velocity at the upper tip of the particle, which increases with the increase of Gr. The effect of the wall repulsion is evaluated via the pressure distribution at the equilibrium state, which is displayed in Fig. 13. Obviously, the pressure between the lower side of the particle and the wall increases with the increase of Gr, resulting in a stronger wall repulsion to balance the gravitational force and thermal effect.

The effect of thermal convection is mainly caused by the cooling of the surrounding fluid due to the temperature difference between the particle surface and the fluid. According to the Boussinesq
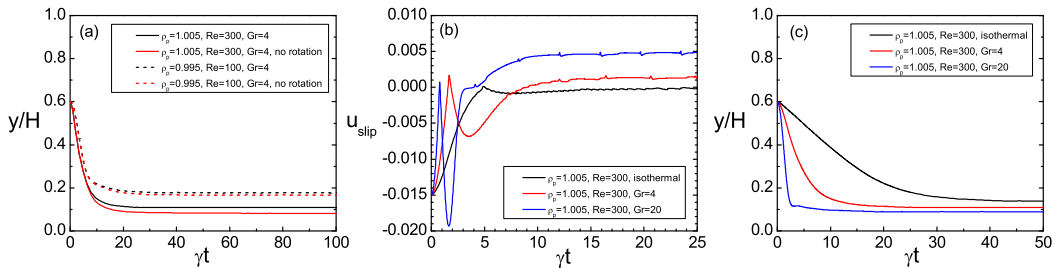

FIG. 12. (a) The effect of particle rotation on the lateral position for different particle densities. Time evolution of the particle's (b) slip velocity and (c) lateral positions for different Grashof numbers.
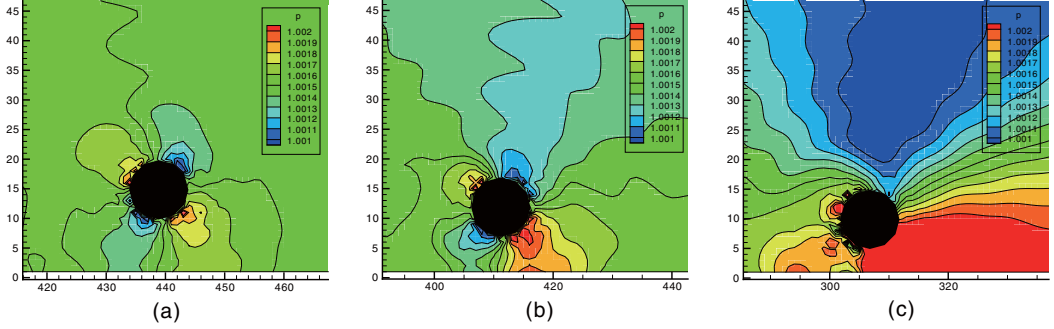
FIG. 13. The pressure distribution of the flow field for (a) isothermal, (b) Gr = 4, and (c) Gr = 20 at the equilibrium state. The particle density is $\rho_p = 1.005$ and the Reynolds number is fixed, Re = 300.

approximation, the density of cold fluid increases and thus moves toward the bottom wall, which induces a downward flow around the particle. Figure 14 illustrates the flow field in the vertical direction at the very early stage ($\gamma t = 2.5$) of the particle migration. Compared with the isothermal case that is only driven by the gravitational force, a conspicuous negative velocity field is formed around the particle in the presence of thermal convection, of which the magnitude rises as the Grashof number increases. Therefore, the particle will drop rapidly toward the bottom wall once it is released in the channel, as can be witnessed from the particle trajectory shown in Fig. 12(c). When the particle gradually reaches its equilibrium position, the wall repulsion and the Saffman lift force as well as the Magnus force, grow larger and become strong enough to balance the gravitational force and the lift force due to thermal convection.

C. Particles with $\rho_p < \rho_f$

In this section, migration behavior of particles that are lighter than the fluid is examined. In the light of the symmetry of the shear flow system, it is anticipated that the equilibrium positions of particles lighter and heavier than the fluid with the same density difference σ are symmetric about the centerline of the channel under the isothermal condition. An diagram identical to that displayed in Fig. 7 can be obtained to decide whether the particle floats up to the top of the channel or remains suspended.

From the previous discussion, it is clear that the downward lift force due to thermal convection is in the same direction as the gravitational force of the particle that is heavier than the fluid. However, when the particle is lighter than the fluid, the gravitational force turns into an upward buoyancy, as
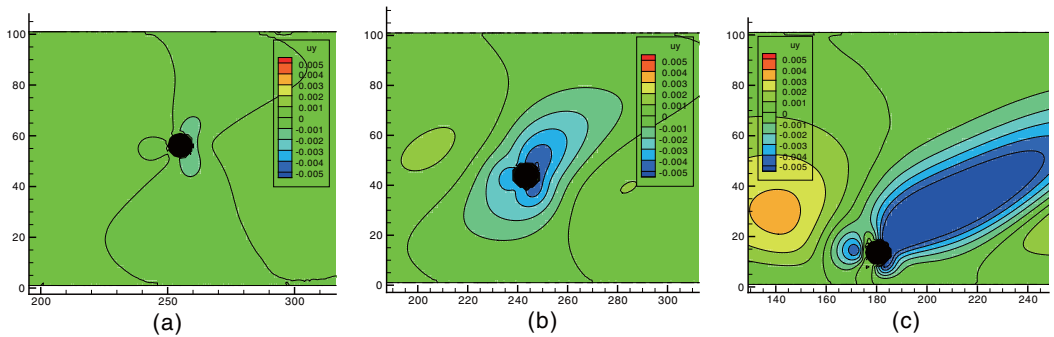

FIG. 14. The vertical velocity contour of the flow field for (a) isothermal, (b) Gr = 4, and (c) Gr = 20 at $\gamma t = 2.5$. The particle density is $\rho_p = 1.005$ and the Reynolds number is fixed, Re = 300.
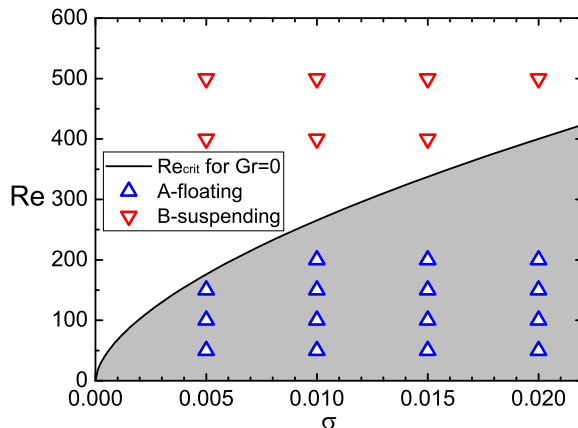
FIG. 15. A regime map showing the two cases studied to explore the effect of thermal convection. The solid line refers to Eq. (34).

revealed in Fig. 11(b), which becomes an opponent of the thermal lift force. Hence, the equilibrium position of the particle mainly results from the competition between the buoyancy and the thermal lift force. To explore the effect of thermal convection, two cases are considered according to the diagram shown in Fig. 7 under the isothermal condition; they are illustrated in Fig. 15. Case A refers to the particle floating to the top (corresponding to the settled regime for a particle heavier than the fluid), and case B denotes the particle that remains suspended in the channel. For each case, the equilibrium positions of the particle with various Grashof numbers are examined.

Figure 16 shows the equilibrium position as a function of Grashof number for case A. It can be seen that with the increase of Gr, the particle first stays at the top wall of the channel and suddenly starts to settle down until a critical Gr is reached. Then the particle gradually moves toward the bottom wall when Gr is further increased. As shown in each subplot in Fig. 16, it is observed that the critical Grashof number that triggers the settling increases with the decrease of particle density when the Reynolds number is fixed. Comparing the results of the same particle density, it is also found that the critical Grashof number also increases with the increase of the Reynolds number. For instance, the critical Grashof numbers for $\rho_p = 0.980$ are $Gr_{crit} = 3.50$, 4.55, and 6.55 for $Re = 50$, 100, and 150, respectively.

Figure 17(a) summarizes the critical Grashof number Gr_{crit} as a function of the dimensionless density ratio σ for different Reynolds numbers. A linear relationship between Gr_{crit} and σ is found for all the Reynolds numbers investigated. The larger the Reynolds number, the larger the slope of the linear function. Furthermore, it is worth noting that all of the linear correlations seem to pass
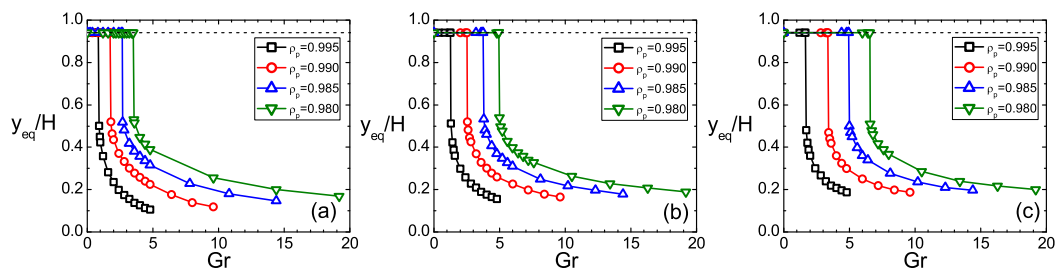

FIG. 16. Equilibrium position as a function of Grashof number for different particle densities and Reynolds numbers: (a) $Re = 50$, (b) $Re = 100$, and (c) $Re = 150$. The dashed line represents the top of the channel.
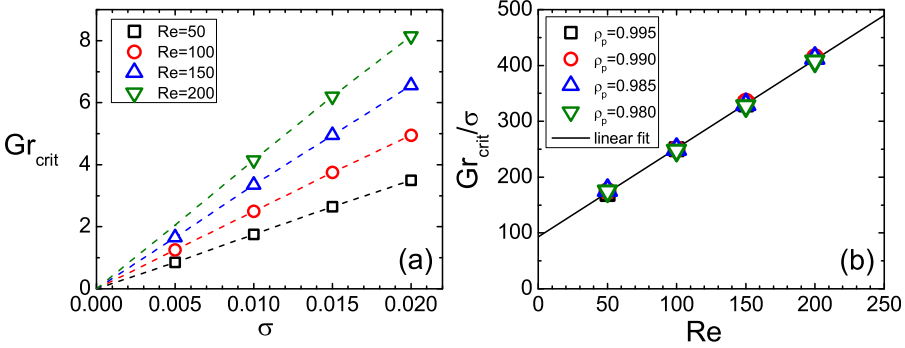
FIG. 17. (a) Critical Grashof number as a function of dimensionless density ratio for different Reynolds numbers. (b) Normalized critical Grashof number as a function of the Reynolds number.

through the origin, implying a rigorously positive proportional relationship between Gr_{crit} and σ. Therefore, another dimensionless parameter can be defined as

$$\lambda_L = \frac{Gr}{\sigma},\tag{38}$$

which characterizes the ratio of the lift force caused by thermal convection to the buoyancy. Figure 17(b) replots the critical value of Gr/σ as a function of Re. It is found that Gr_{crit}/σ for different particle densities all collapse and a master linear relationship is obtained between Gr_{crit}/σ and Re,

$$\lambda_{L,crit} = c_5 Re + c_6,\tag{39}$$

where the fitting parameters are $c_5 = 1.59$ an $c_6 = 9.31$ in the current study. According to the above discussion, the lift force due to thermal convection is downward while the buoyancy is upward, and the balance between these two forces determines the equilibrium position of the particle. With the increase of σ, i.e., the particle is lighter, the buoyancy becomes stronger. Thus a larger thermal lift force is required to trigger the settling of the particle, leading to a higher Re_{crit}. A close examination of Fig. 17(b) reveals that the dominating parameter to describe the particle's equilibrium position can be universally defined as Gr/σ for various particle densities, and the critical value is the same when the Reynolds number remains unchanged.
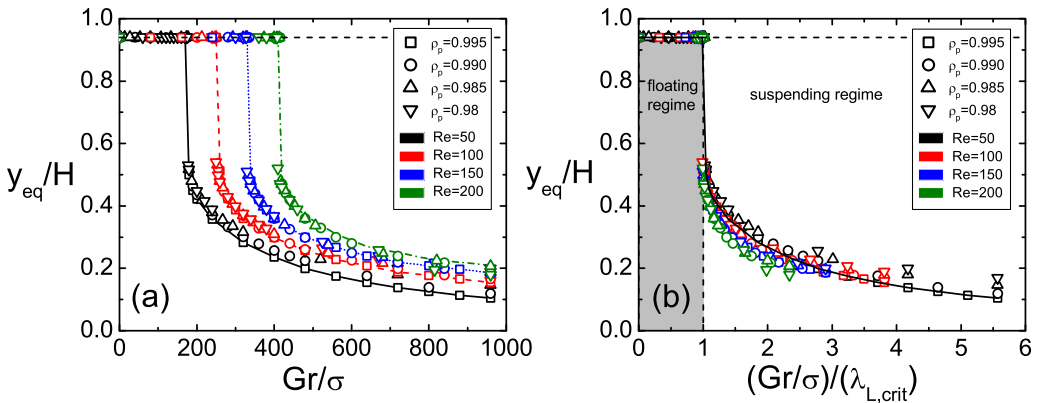

FIG. 18. Equilibrium position as a function of (a) Gr/σ and (b) $\frac{Gr/\sigma}{\lambda_{L,crit}}$ for different particle densities and Reynolds numbers in case A.
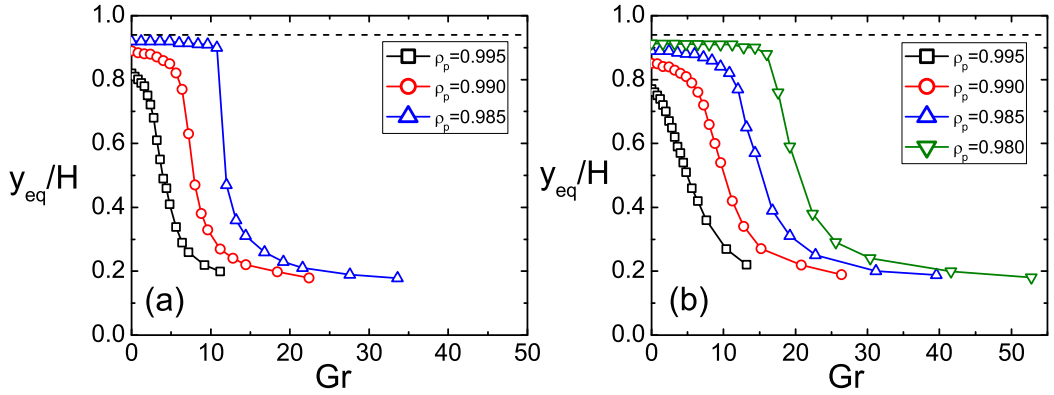
FIG. 19. Equilibrium position as a function of Grashof number for different particle densities and Reynolds numbers: (a) Re = 400 and (b) Re = 500. The dashed line represents the top of the channel.

Then the new parameter Gr/σ is employed to replot the data in Fig. 16, and the results are shown in Fig. 18(a). It can be seen that the equilibrium positions of different particle densities are well regressed with Gr/σ for each Reynolds number. With the increase of Re, the equilibrium position profile shifts toward the right, giving rise to a larger critical value of Gr/σ. If we further normalize the data with the empirical critical value $\lambda_{L,crit}$ obtained in Eq. (39), a universal description can be obtained, which is revealed in Fig. 18(b). It is observed that the equilibrium positions for different particle densities and Reynolds numbers all collapse on a single master curve, where a critical value is identified as $(Gr_{crit}/\sigma)/\lambda_{L,crit} = 1$ to distinguish two regimes, i.e., floating and suspending. When $(Gr_{crit}/\sigma)/\lambda_{L,crit} < 1$, the particle stays at the top wall, and it starts to settle due to thermal convection and remains suspended in the channel as $(Gr_{crit}/\sigma)/\lambda_{L,crit} > 1$. With the increase of the parameter $(Gr_{crit}/\sigma)/\lambda_{L,crit}$, the equilibrium position gradually moves toward the bottom wall.

For case B, the equilibrium positions of the particle are presented in Fig. 19. Different from case A, the particle at $Gr = 0$ does not stay at the top wall, but remains suspended at a position depending on the Reynolds number and density, as shown in Fig. 7. With the increase of the Grashof number, the equilibrium position moves smoothly toward the bottom of the channel, where the sudden occurrence of the settling is not observed. It is noted that the variation of equilibrium
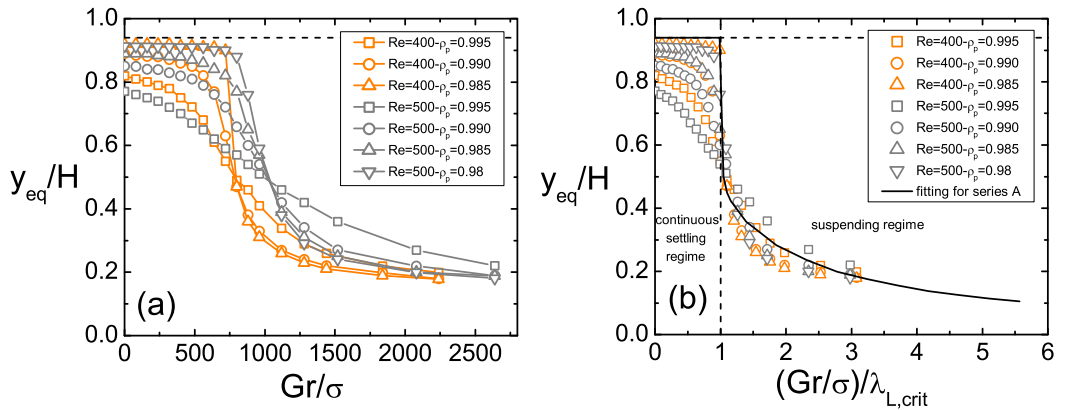

FIG. 20. Equilibrium position as a function of (a) Gr/σ and (b) $\frac{Gr/\sigma}{\lambda_{L,crit}}$ for different particle densities and Reynolds numbers for case B.

position of a particle with $\rho_p = 0.985$ at Re $= 400$ seems to resemble that for case A, because this particular case locates close to the critical line shown in Fig. 15. In order to compare with case A, the same dimensionless parameters Gr$/\sigma$ and (Gr$/\sigma)/\lambda_{L,\text{crit}}$ are applied to reanalyze the results, which are shown in Fig. 20. From Fig. 20(a) it can be seen that the equilibrium position profiles of the same Reynolds number are not well regressed on the same curve in terms of Gr$/\sigma$, indicating a different scaling of the particle's equilibrium position. Figure 20(b) further shows the regression of equilibrium position with respect to (Gr$/\sigma)/\lambda_{L,\text{crit}}$, where the fitting of case A is included for comparison. It is interesting that the variation of the equilibrium position when (Gr$/\sigma)/\lambda_{L,\text{crit}} > 1$ appears to follow a similar pattern to case A. However, the equilibrium positions with (Gr$/\sigma)/\lambda_{L,\text{crit}} < 1$ are not well depicted with a single curve. The variation depends on the Reynolds number and the particle density. Therefore, two different regimes for case B can be defined in a similar way, i.e., a suspending regime with (Gr$/\sigma)/\lambda_{L,\text{crit}} > 1$ and a continuous settling regime with (Gr$/\sigma)/\lambda_{L,\text{crit}} < 1$.

V. CONCLUSIONS

In this study, inertial migration of a non-neutrally buoyant particle in simple shear flows in the presence of thermal convection is numerically analyzed using a double-population lattice Boltzmann method. The particle density considered is in the range of $\rho_p = 0.98 - 1.02$ and the channel Reynolds number is up to 500. The effect of thermal convection is tuned by systematically varying the Grashof number, which is in the range of Gr $= 0 - 55$. Under the isothermal condition (Gr $= 0$), the particle with a fixed density either settles to the bottom of the channel ($\rho_p > \rho_f$) or floats to the top ($\rho_p < \rho_f$) when the Reynolds number is below a critical value, above which the particle becomes suspended due to the inertial lift force. The relationship between the critical Reynolds number and the particle density can be well described by a power law with an exponent of 0.59. However, in the presence of thermal convection, the migration behavior of the particle is dependent on whether its density is larger or smaller than the fluid's. For a particle heavier than the fluid, the settling is enhanced by thermal convection because of the synergistic effect of the downward thermal lift force and the gravitational force. As a result, the critical Reynolds number to lift the particle to be suspended increases and can be depicted with a linear function of the dimensionless density ratio σ within the range $\sigma = 0 - 0.02$. On the other hand, for a particle lighter than the fluid, the variation of the equilibrium position as a function of the Grashof number depends on whether it floats to the top wall or remains suspended at Gr $= 0$. For a particle that floats to the top, it will suddenly settle down and become suspended when the Grashof number is increased above a critical value. It is discovered that the critical Grashof number for different particle densities is a unique function of a normalized form Gr$/\sigma$, which increases linearly with the increase of Reynolds number. Furthermore, an empirical dimensionless number is proposed as (Gr$/\sigma)/\lambda_{L,\text{crit}} = $ (Gr$/\sigma)/(1.59$Re $+ 9.31)$ in order to distinguish the floating and suspending of the particle. When (Gr$/\sigma)/\lambda_{L,\text{crit}} < 1$, the particle stays at the top wall. When (Gr$/\sigma)/\lambda_{L,\text{crit}} > 1$, the particle becomes suspended in the channel and its equilibrium position gradually moves toward the bottom wall. However, for particles initially suspended in the channel at Gr $= 0$, the critical settling behavior is not observed anymore. Instead, the particle's equilibrium position moves continuously from a position below the top wall toward the bottom wall with the increase of the Grashof number.

ACKNOWLEDGMENTS

[1] D. L. Koch and R. J. Hill, Inertial effects in suspension and porous-media flows, Annu. Rev. Fluid Mech. **33**, 619 (2001).

[2] A. A. S. Bhagat, S. S. Kuntaegowdanahalli, and I. Papautsky, Inertial microfluidics for continuous particle filtration and extraction, Microfluid. Nanofluid. **7**, 217 (2009).

[3] Y. W. Kim and J. Y. Yoo, Three-dimensional focusing of red blood cells in microchannel flows for bio-sensing applications, Biosens. Bioelectron. **24**, 3677 (2009).

[4] S. Chen, S. Li, and J. S. Marshall, Exponential scaling in early-stage agglomeration of adhesive particles in turbulence, Phys. Rev. Fluids **4**, 024304 (2019).

[5] S. Chen and S. Li, Collision-induced breakage of agglomerates in homogenous isotropic turbulence laden with adhesive particles, J. Fluid Mech. **902**, A28 (2020).

[6] M. Wei, Y. Zhang, X. Luo, X. Li, X. Xu, and Z. Zhang, Graphite dust deposition on HTGR steam generator: Effects of particle-wall and particle-vortex interactions, Nucl. Eng. Des. **330**, 217 (2018).

[7] D. Di Carlo, D. Irimia, R. G. Tompkins, and M. Toner, Continuous inertial focusing, ordering, and separation of particles in microchannels, Proc. Natl. Acad. Sci. USA **104**, 18892 (2007).

[8] J. M. Martel and M. Toner, Inertial focusing in microfluidics, Annu. Rev. Biomed. Eng. **16**, 371 (2014).

[9] H. Udono and M. Sakai, A numerical study on dynamic inertial focusing of microparticles in a confined flow, Granular Matter **19**, 79 (2017).

[10] G. Segré and A. Silberberg, Radial particle displacements in Poiseuille flow of suspensions, Nature **189**, 209 (1961).

[11] P. G. T. Saffman, The lift on a small sphere in a slow shear flow, J. Fluid Mech. **22**, 385 (1965).

[12] B. P. Ho and L. G. Leal, Inertial migration of rigid spheres in two-dimensional unidirectional flows, J. Fluid Mech. **65**, 365 (1974).

[13] P. Vasseur and R. G. Cox, The lateral migration of a spherical particle in two-dimensional shear flows, J. Fluid Mech. **78**, 385 (1976).

[14] J. A. Schonberg and E. J. Hinch, Inertial migration of a sphere in Poiseuille flow, J. Fluid Mech. **203**, 517 (1989).

[15] P. Cherukat, J. B. McLaughlin, and A. L. Graham, The inertial lift on a rigid sphere translating in a linear shear flow field, Int. J. Multiphase Flow **20**, 339 (1994).

[16] J. Feng, H. H. Hu, and D. D. Joseph, Direct simulation of initial value problems for the motion of solid bodies in a Newtonian fluid. Part 2. Couette and Poiseuille flows, J. Fluid Mech. **277**, 271 (1994).

[17] E. S. Asmolov, The inertial lift on a spherical particle in a plane Poiseuille flow at large channel Reynolds number, J. Fluid Mech. **381**, 63 (1999).

[18] Z. G. Feng and E. E. Michaelides, Equilibrium position for a particle in a horizontal shear flow, Int. J. Multiphase Flow **29**, 943 (2003).

[19] J. P. Matas, J. F. Morris, and É. Guazzelli, Inertial migration of rigid spherical particles in Poiseuille flow, J. Fluid Mech. **515**, 171 (2004).

[20] J. Matas, J. Morris, and É. Guazzelli, Lateral force on a rigid sphere in large-inertia laminar pipe flow, J. Fluid Mech. **621**, 59 (2009).

[21] C. A. Hieber and B. Gebhart, Mixed convection from a sphere at small Reynolds and Grashof numbers, J. Fluid Mech. **38**, 137 (1969).

[22] E. Bar-Ziv, B. Zhao, E. Mograbi, D. Katoshevski, and G. Ziskind, Experimental validation of the Stokes law at nonisothermal conditions, Phys. Fluids **14**, 2015 (2002).

[23] H. Gan, J. Chang, J. J. Feng, and H. H. Hu, Direct numerical simulation of the sedimentation of solid particles with thermal convection, J. Fluid Mech. **481**, 385 (2003).

[24] E. Mograbi and E. Bar-Ziv, Dynamics of a spherical particle in mixed convection flow field, J. Aerosol Sci. **36**, 387 (2005).

[25] K. Walayat, Z. Zhang, K. Usman, J. Chang, and M. Liu, Dynamics of elliptic particle sedimentation with thermal convection, Phys. Fluids **30**, 103301 (2018).

[26] S. Li, J. Xie, M. Dong, and L. Bai, Rebound characteristics for the impact of SiO_2 particle onto a flat surface at different temperatures, Powder Technol. **284**, 418 (2015).

[27] M. Wei, Y. Zhang, Z. Fang, X. Wu, and L. Sun, Graphite aerosol release to the containment in a water ingress accident of high temperature gas-cooled reactor (HTGR), Nucl. Eng. Des. **342**, 170 (2019).

[28] Z. Yu, X. Shao, and A. Wachs, A fictitious domain method for particulate flows with heat transfer, J. Comput. Phys. **217**, 424 (2006).

[29] Z. G. Feng and E. E. Michaelides, Inclusion of heat transfer computations for particle laden flows, Phys. Fluids **20**, 040604 (2008).

[30] D. Y. Kim, H. S. Yoon, and M. Y. Ha, Particle behavior in a vertical channel with thermal convection in the low Grashof number regime, Comput. Fluids **48**, 183 (2011).

[31] Z. Hashemi, O. Abouali, and R. Kamali, Three dimensional thermal lattice Boltzmann simulation of heating/cooling spheres falling in a Newtonian liquid, Int. J. Therm. Sci. **82**, 23 (2014).

[32] B. Yang, S. Chen, C. Cao, Z. Liu, and C. Zheng, Lattice Boltzmann simulation of two cold particles settling in Newtonian fluid with thermal convection, Int. J. Heat Mass Transfer **93**, 477 (2016).

[33] J. Hu and Z. Guo, A numerical study on the migration of a neutrally buoyant particle in a Poiseuille flow with thermal convection, Int. J. Heat Mass Transfer **108**, 2158 (2017).

[34] R. Safa, A. S. Goharrizi, S. Jafari, and E. J. Javaran, On the evaluation of heat and mass transfer effects on the migration behavior of neutrally buoyant particles in a Couette flow, Int. J. Heat Mass Transfer **144**, 118659 (2019).

[35] B. Metzger, O. Rahli, and X. Yin, Heat transfer across sheared suspensions: Role of the shear-induced diffusion, J. Fluid Mech. **724**, 527 (2013).

[36] H. Zhang, H. Benoit, I. Perez-Lopèz, G. Flamant, T. Tan, and J. Baeyens, High-efficiency solar power towers using particle suspensions as heat carrier in the receiver and in the thermal energy storage, Renewable Energy **111**, 438 (2017).

[37] A. Calderón, A. Palacios, C. Barreneche, M. Segarra, C. Prieto, A. Rodriguez-Sanchez, and A. I. Fernández, High temperature systems using solid particles as TES and HTF material: A review, Appl. Energy **213**, 100 (2018).

[38] J. A. Almendros-Ibáñez, M. Fernández-Torrijos, M. Daz-Heras, J. F. Belmonte, and C. Sobrino, A review of solar thermal energy storage in beds of particles: Packed and fluidized beds, Sol. Energy **192**, 193 (2019).

[39] P. L. Bhatnagar, E. P. Gross, and M. Krook, A model for collision processes in gases. I. Small amplitude processes in charged and neutral one-component systems, Phys. Rev. **94**, 511 (1954).

[40] Y. H. Qian, D. d'Humières, and P. Lallemand, Lattice BGK models for Navier-Stokes equation, Europhys. Lett. **17**, 479 (1992).

[41] S. Chen and G. D. Doolen, Lattice Boltzmann method for fluid flows, Annu. Rev. Fluid Mech. **30**, 329 (1998).

[42] Z. Guo, B. Shi, and C. Zheng, A coupled lattice BGK model for the Boussinesq equations, Int. J. Numer. Methods Fluids **39**, 325 (2002).

[43] Z. Guo, C. Zheng, and B. Shi, Discrete lattice effects on the forcing term in the lattice Boltzmann method, Phys. Rev. E **65**, 046308 (2002).

[44] H. Chen, S. Chen, and W. H. Matthaeus, Recovery of the Navier-Stokes equations using a lattice-gas Boltzmann method, Phys. Rev. A **45**, R5339 (1992).

[45] D. Yu, R. Mei, L. S. Luo, and W. Shyy, Viscous flow computations with the method of lattice Boltzmann equation, Prog. Aerosp. Sci. **39**, 329 (2003).

[46] C. Peng, Y. Teng, B. Hwang, Z. Guo, and L. P. Wang, Implementation issues and benchmarking of lattice Boltzmann method for moving rigid particle simulations in a viscous flow, Comput. Math. Appl. **72**, 349 (2016).

[47] T. Zhang, B. Shi, Z. Guo, Z. Chai, and J. Lu, General bounce-back scheme for concentration boundary condition in the lattice-Boltzmann method, Phys. Rev. E **85**, 016701 (2012).

[48] A. J. C. Ladd, Sedimentation of homogeneous suspensions of non-Brownian spheres, Phys. Fluids **9**, 491 (1997).

[49] W. Liu and C. Y. Wu, Analysis of inertial migration of neutrally buoyant particle suspensions in a planar Poiseuille flow with a coupled lattice Boltzmann method-discrete element method, Phys. Fluids **31**, 063301 (2019).

[50] W. Liu and C. Y. Wu, Migration and agglomeration of adhesive micro-particle suspensions in a pressure-driven duct flow, AIChE J. **66**, e16974 (2020).

[51] W. Liu and C. Y. Wu, Modelling complex particle–fluid flow with a discrete element method coupled with lattice Boltzmann methods (DEM-LBM), ChemEng. **4**, 55 (2020).

[52] W. Liu and C. Y. Wu, Lateral migration of a neutrally buoyant particle in Couette flow with thermal convection, Int. J. Multiphase Flow **138**, 103612 (2021).